Imperial College London

Department of Bioengineering

Effect of Agent Concentration in Ultrasound Super-Resolution Imaging at Clinically Low Frequency

Mphil Thesis

Zhu, Ziyan [redacted]

Supervisor: Prof Mengxing Tang

Date: 2021.12 Word count: 11863

Statement of Originality

The work presented in this thesis is my own and that all else is appropriately referenced.

ZIYAN ZHU
June 2021

Copyright Declaration

Abstract–Imaging of microvasculature can be valuable for the diagnosis and treatment monitoring of cancer and other diseases. Ultrasound has the potential due to its excellent spatial and temporal resolution. Super-resolution ultrasound imaging using contrast enhanced ultrasound localization microscopy is able to visualize microvasculature beyond the wave diffraction limit. The microbubble based super-resolution depends on controlling the bubble concentration, which needs to be low enough to locate isolated microbubbles. However too low a concentration will prolong the data acquisition. The aim of the thesis was to evaluate the impact of microbubble concentration on super-resolution ultrasound imaging, and to improve the signal processing in super-resolution imaging. First, various concentrations of microbubble contrast agents (6×10^3 to 1.5×10^6 particles/ml) were injected into a 200 microns cross-tube flow phantom. The experimental results show that the concentration affects the resolution of the cross-tube images. When the concentration is lower than the 1.5×10^5particles/ml, two tubes in a selected region of interest near the intersection that are 370 microns apart can be separated, which is close to the expected distance (390 microns). Second, the comprehensive effects of data acquisition time and concentration on imaging resolution were studied. The preferred range of concentration was determined between 1.5×10^4 to 6×10^4particles/ml. This result can be used to better inform data acquisition in the further research. Third, a weight adaptive denoising method based on morphology was developed to remove noises which were produced in the step of microbubble detection at the preferred range of concentration. Therefore, the resolution and the accuracy of the velocity map were further improved.

Index Terms –microbubbles, super-resolution, ultrasound imaging, concentration, denoising

List of abbreviations

Magnetic resonance imaging -- MRI
Computed tomography -- CT
High frame-rate -- HFR
Frames per second -- FPS
Graphical processing unit -- GPU
Signal-to-noise-ratio -- SNR
Contrast-enhanced ultrasound imaging -- CEUS
Pulse inversion -- PI
Amplitude modulation -- AM
Pulse inversion amplitude modulation -- PIAM
Singular value decomposition -- SVD
Photoactivated localization microscopy -- PALM
Differential imaging -- DI
Stochastic optical reconstruction microscopy -- STORM
Ultrasound localization microscopy -- ULM
Point spread function -- PSF
Full width at half maximum -- FWHM
Time gain compensation -- TGC
Delay and sum -- DAS
Radio frequency -- RF
Region of interest -- ROI
Standard deviation -- STD

Acknowledgements

First of all, I would like to express my heartfelt thanks to my supervisor Profesor Mengxing Tang for offering me the opportunity to study in our ULIS group, as well as for his concern, help, support and cultivation during my study life. He encouraged me on every little discovery I made and supported me in asking even the most basic questions. At the beginning of the experiment, he personally led us beginners to set up the experimental platform. He provided an excellent academic environment and passed on his enthusiasm for scientific research to me. Training in our world-leading research group is a very precious experience in my life and I believe it will lay a good foundation for my future development.

Secondly, I wish to thank all the members in our ULIS group for their help. Thanks to all the people for giving me help and encouragement that I have met during my study life. Especially for Ge Zhang, Kai Riemer, Joseph Hansen-Shearer, Xinhuan Zhou, Bingxue Wang, Xiaowei Zhou. During my experiment, they taught me how to use the experimental equipment and are very patient to give me advice when I encounter difficulties.

Finally, many thanks go to my parents and boyfriend for their concern and support. During this training, I also realized some of my own shortcomings. Thank you for them to help me find problems and always remind me to make corrections.

Contents

1. Background

1.1 Microvascular Imaging

Microvasculature imaging is a major challenge in clinical imaging. Although a variety of imaging modalities, including magnetic resonance imaging (MRI), computed tomography (CT), ultrasound and nuclear imaging have shown great value in medical diagnosis, these methods are still limited by their sub-millimeter or millimeter resolution in deep tissue. Resolutions are not sufficient to distinguish the microvasculature [1].

In cancer patients, sustained angiogenesis has been observed in the early-stage pathogenesis of cancers. Usually, it is difficult for malignant tumors to be noticed until the lesion has become large enough. However, tumors can potentially be detected early from the stage of discernable microvessel growth by applying novel imaging methods. Commonly, the diameter of tumor microvessel is smaller than healthy vessels, with a diameter of less than 60 μm. Morphologically, tumor microvessels are more tortuous and have more complex structures[2]. Such imaging methods could be valuable for auxiliary diagnosis such as using density quantification,and monitoring the cancer treatment such as antiagiogenesis therapy, which enables timely adjustment and bring a better prognosis of patients [3]. Therefore, a high-resolution imaging technique that is able to visualize microvessels is required.

1.2 Ultrasound Imaging

Ultrasound imaging has been a widely used imaging method in the field of medical diagnostics for half a century due to its safety, accessibility, affordability, and excellent spatial and temporal resolution. In 2D B-Mode images human tissues and organs can be observed, which are reconstructed from echoes. These echoes emerge due to reflections and scatterings after the ultrasound pulse encounters boundaries of tissues and small scatters. The brightness of the image is related to the strength or amplitude of the signal. The resolution of traditional ultrasound is subject to the diffraction limit. In theory, the best resolution of the ultrasound imaging is up to half-wavelength [4]. The resolution of the ultrasound imaging will increase when the frequency rises, but at the same time the attenuation of ultrasound will also increase. The attenuation ultimately diminishes the penetration depth of high-frequency ultrasound and medical diagnosis of human or animal can often require imaging depth of 10cm or greater [5]. Furthermore, the actual resolution of ultrasound imaging is restricted by the point spread function of an ultrasound system, which lowers the actual resolution of ultrasound imaging compared to the theoretical resolution limit. The point spread function describes the response of the imaging system to a point source, which represents the characteristics of the imaging system. The frequency and point spread function restrict the resolution of an ultrasound imaging.

A recent advancement in medical diagnosis ultrasound imaging is the development of high frame-rate (HFR) ultrasound imaging technique [6]. This technique is based on transmitting a

plane or diverging wave over a wide field of view and parallel beamforming processing instead of the conventional line-by-line sweeping of focused wave imaging [6][7-8]. With that the speed of data acquisition has been increased to over 1000 frames per second (fps) from 30-40fps. This technique has been employed in clinical application with graphical processing unit (GPU)-based platforms [9]. Moreover, for the problem of reduced image signal-to-noise-ratio (SNR) and decreased contrast resulted by the lack of focusing, images which are acquired through coherent compounding of data with varied steering angles are able to compensate for this lack of focusing and improve the SNR and contrast of image [10]. Although an HFR system improves data acquisition speed while ensuring the image quality, there is still no fundamental improvement in resolution in ultrasound imaging.

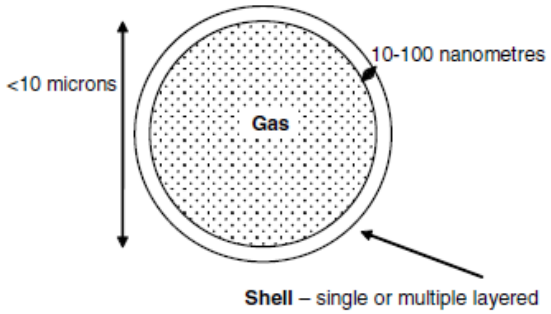

Fig. 1. Microbubble model [4]

1.3 Contrast-Enhanced Ultrasound Imaging

With the use of contrast agents, contrast-enhanced ultrasound imaging (CEUS) makes the visualization of more information possible. Among ultrasound contrast agents, the most used one is microbubble. A microbubble is a gas-filled sphere encapsulated in a single- or multiple-layered shell of proteins or lipids, commonly less than 10μm in diameter shown in Fig. 1[4]. Such gas-filled microbubbles can result in a stronger scattering echo signal than liquid or solid filled particles of the same size. High backscattered signals from microbubbles enhance the scattering echoes of blood flow in the blood circulation, which increases the effect of ultrasound imaging. The intensity of backscattered signals depends on the size of microbubbles [11]. The larger the size is, the stronger the signal will be. In addition, each microbubble vibrates most readily and the backscattered signal can reach the highest level when ultrasound frequency is the same as the resonant frequency of the microbubble [12]. Resonant frequency of microbubble is determined by the bubble size and the type of the shell. Furthermore, instead of quickly dissolve, microbubbles can exist in the blood for a period of time due to the protection of the shell. The time of persistence and response to ultrasound of microbubbles are determined by the composition of the shell.

Various CEUS imaging techniques have been proposed. Pulse inversion (PI) imaging can filter linear signals through sending a pulse and a reverse pulse, adding their echoes together to leave contrast signals. This method overcomes the bandwith limitation of second-harmonic imaging. Similar to PI, an amplitude modulation (AM) method keeps the difference nonlinear signal through transmitting half-amplitudes, full-amplitudes and half-amplitudes pulses orderly

and subtracting the echo of full-amplitudes from the two half-amplitudes. Pulse inversion amplitude modulation (PIAM) method combines PI and AM, which can obtain more sensitive signal. In the study by Zhu et al. [7], for various bubble detection methods, PI and the singular value decomposition (SVD) filter methods have been compared in an experiment that SVD filter can obtain the signals of bubbles in the bottom tube while remove the signals of the top tube that PI cannot.

1.4 Ultrasound Super-Resolution Imaging

Inspired by the principle of fluorescence photoactivated localization microscopy (PALM) and stochastic optical reconstruction microscopy (STORM), which has been awarded the 2014 Nobel Prize in chemistry, Couture demonstrated the earliest ultrasound localization microscopy (ULM) in 2010 by using contrast agents instead of fluorescent beacons and an ultrafast ultrasound scanner instead of a camera [5], but super-resolution was not demonstrated. Several CEUS imaging using the ULM method to obtain super-resolution imaging which have been proposed in recent years have overcome the bottle neck in traditional diffraction limits to obtain higher resolution beyond the limitation of the point spread function of ultrasound systems [13-18]. This technique scans a series of frames with sparse microbubbles in each frame by an ultrasound transducer. These frames with sparse microbubbles are obtained through controlling the concentration of microbubbles [2][14][18] or bursting microbubbles subpopulations [15]. The main assumption of this method is that these sparse microbubbles are spatially isolated. Therefore, sub-diffraction images can be obtained through localization processing to identify the center of the corresponding echo from each isolated microbubble and accumulate all the localizations in many frames. This is the basic principle of super-resolution ultrasound imaging. As this technique is not affected by the diffraction limit, microbubble based super-resolution ultrasound imaging can further improve the imaging ability.

In general, the imaging procedure of super-resolution ultrasound imaging consists of 6steps including acquisition, detection, isolation, localization, tracking and mapping. For acquisition, data can be obtained using traditional B-mode or ultrafast ultrasound imaging. In clinical data processing, a two-stage motion estimation method has been proposed to correct the motion between each frame, which increases the accuracy of super-resolution [19]. Brown et al. [2] has compared the localization accuracy and contrast-to-tissue ratio among differential imaging (DI), pulse inversion (PI) and singular value decomposition (SVD), and the result show that PI is suitable for tumor microvasculature imaging. Except for the traditional concentration control method to maintain the single-microbubble localization, sparsity-based methods [20] and deep learning based methods [21] have been proposed so that higher concentrations can be permitted. Christensen-Jeffries et al. [22] has compared microbubble axial localization errors of centroid, onset, 50%-point, peak, Gsn and Gsn Fixed localization methods. Different tracking methods such as multiple microbubbles [23], graph-based [24] and kalman filter- based methods [25] have been proposed.

At present, although there are many encouraging studies showing the improvement in super-resolution ultrasound imaging using microbubbles contrast agents, this method depends on controlling the concentration of microbubble in a low range to obtain spatially independent

microbubble clouds. For the intersection of the cross-tube, localization errors, which are caused by the overlapped microbubble clouds in two tubes, are easy to occur at high concentrations. This situation will decrease the resolution at the intersection. High concentration will cause microbubble clouds to overlap, which will result in errors in localization. But if the concentration is too low, it needs a relatively long data acquisition time, which will increase the motion artifacts. In addition, at too low concentrations, it creates a challenge for the current commonly used microbubble detection method (SVD). Some erroneous signals which SVD failed to filter out will bring noises in the final super-resolved images [5]. The preferred concentration range is also affected by these noises, which will lead to mistaking noises as microbubble clouds.

In this thesis, firstly, the effect of concentration of microbubble contrast agent on the resolution of the super-resolution has been demonstrated experimentally. Secondly, the comprehensive effects of data acquisition time and concentration on imaging resolution have been studied and the preferred concentration has been selected within the studied range. Finally, for the noises that were produced after using the microbubble detection method, especially at low concentrations, a denoising method has been developed to effectively remove these noises. Therefore, the imaging accuracy, the resolution of the super-resolution, and also the accuracy of the velocity map was improved.

2. Method

2.1 Cross-tube Phantom Fabrication

The cross-tube flow phantom shown in Fig. 2 has been designed to perform this experiment. The main part of the cross-tube phantom consists of two crossed 200-μm-cellulose tubes (Platinum Cured Silicone Tubing, Harvard Apparatus UK, Cambridge, UK) with the internal diameter of 200±15μm and the thickness of the wall is 8±1μm in the dry state, which is set as the ground truth of the imaging. Tubes are ultra-pure biocompatible and the material of tubes are silicone, which are non-toxic and non-hemolytic. In consideration of the practical difficulty in the experiment that tubes need to be fixed and the contrast agent needs to be continuously injected into tubes, tubes with diameters of 200 microns were selected for making the phantom. Two syringes were used to inject microbubble contrast agent into tubes. Because the diameter of the 200-μm-cellulose tube is too small, in order to match the size of the needle tubing of syringe, a 300-μm-cellulose tube is needed to connect both ends of the 200-μm-cellulose tube so that the contrast agent can be injected into the 200-μm-cellulose tube. Tubes with diameters of 300 microns were able to match the needle of syringe, which allowed the contrast agent to be fully injected. The ends of the two 200-μm-cellulose tubes were inserted into a 300-μm-cellulose tube of around 1 cm and sealed with a superglue. These four 300-μm-cellulsose tubes pass through four support frames. Each of the support frames composed of three pipette tips that were nested together, which aims to fine-tune the angle of cross-tubes to make sure that the probe and cross-tube were able to place in the same plane.

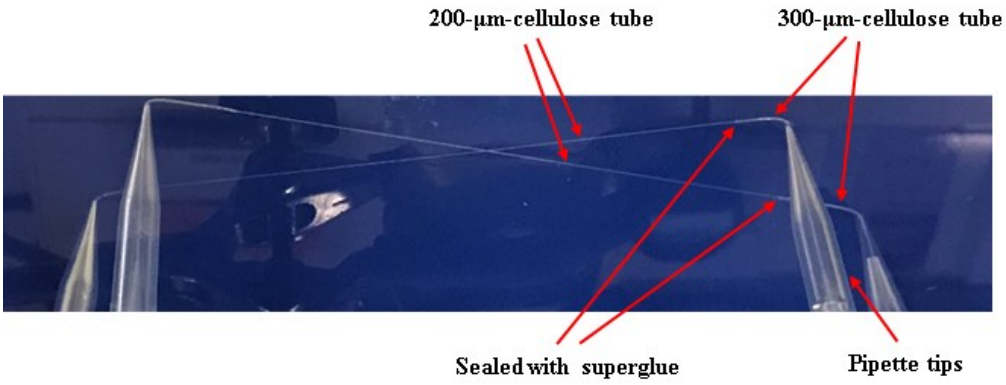

Fig. 2. Cross-tube flow phantom

2.2 Experiment Setup

The left end of the cross-tube (left 300-µm-cellulose tube) was connected to the two syringes and the right end (right 300-µm-cellulose tube) was put in two empty beakers respectively. These two syringes were controlled by a speed-controlled pump (Harvard Apparatus Programmable PHD2000 pump, Harvard Apparatus UK, Cambridge, UK). The speed of the pump was set at 200 µl/min. According to the cross section of the 200 µm tube, the flow rate in the tube was about 100 mm/s. The diluted microbubble liquid was injected into two syringes from containers by the control of the pump at a certain speed. Two absorbers were placed directly below the cross-tube phantom and on the side of the tank to prevent ultrasound artifacts generated by the reflection of the tank. The center of the cross-tube was set at 50mm from the transducer. The ultrasound research platform (Verasonics Vantage 128, Kirkland, WA, USA) and P4-1v probe was used as shown in Fig. 3. The used transmit frequency of the probe was 3.5MHz. The advantage of low frequency probe is that low frequency ultrasound has a better penetration depth, and microbubbles have stronger backscatter signals under low frequency.

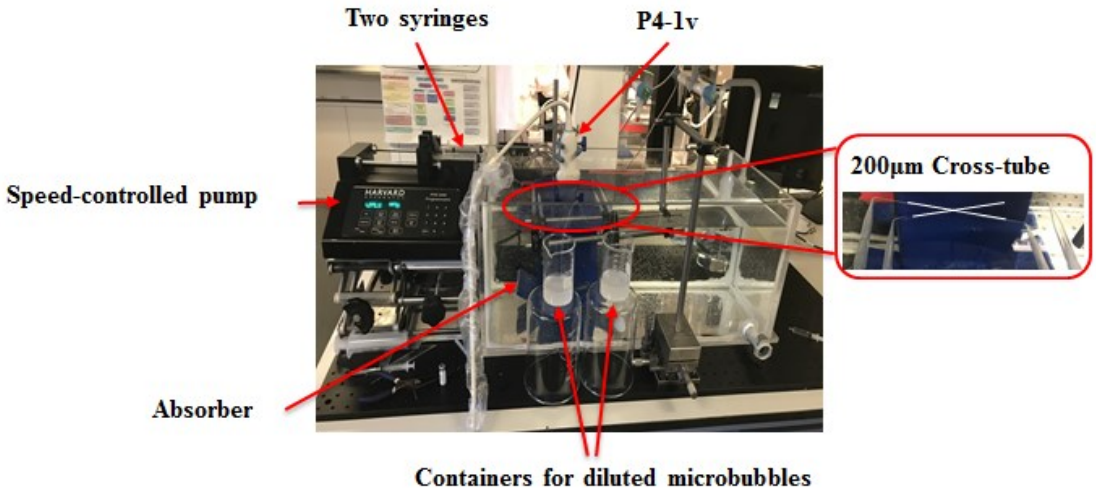

Fig. 3.Experiment setup

2.3 Microbubble Contrast Agent Fabrication

(a) (b) (c)

Fig. 4.(a) A vial of lipid colloid. (b) Octafluoropropane gas. (c)A vial of microbubble contrast agent

The contrast agent which was used in this experiment is microbubble. A vial of lipid colloid (shown in Fig. 4(a)) was filled with Octafluoropropane gas (shown in Fig. 4(b)) via an inlet needle for 30s and accompanied by depressurization through a vent needle. After the gas filling, a bubble shaker was used to agitate the vial at 4000 r/min for 60s to obtain microbubble contrast agent with the estimated concentration of $(3.4 \pm 0.4) \times 10^9$particles/ml and mean diameter 1.12 ± 0.36μm shown in Fig. 4(c) [26].

The concentrations which were selected in 3.3 and 3.4 are shown in table 1.

Table. 1. Concentration dilution ratio of the microbubble contrast agent which was selected in this thesis.

Concentration (particles/ml)	$\mathbf{1.5 \times 10^6}$	$\mathbf{6 \times 10^5}$	$\mathbf{1.5 \times 10^5}$	$\mathbf{6 \times 10^4}$	$\mathbf{1.5 \times 10^4}$	$\mathbf{6 \times 10^3}$
Dilution Ratio (Folds)	2000	5000	20000	50000	200000	500000

2.4 Calibration of Ultrasound System

The diffraction limited resolution of the ultrasound system is measured to characterise the ultrasound imaging system resolution. The system point spread function (PSF) describes the response of the imaging system used to a point source, which is performed to measure the diffraction limited resolution and localization precision in this thesis. A wire with 50 μm diameter was fixed horizontally in the water tank along the elevational direction of the probe. Therefore, at the intersection area between the wire and the axial-lateral imaging plane of the probe, a metal disc with the diameter of 50 μm is obtained to simulate a point scatter. The quality of the imaging system which is used is determined by measuring the diffusion or blurring of this point source. An

ideal point source should be used to measure the point spread function of the system. The theoretical resolution of the ultrasound which is used in this thesis with the frequency of 3.5MHz is 220 microns. The wire with the diameter of 50 microns is far less than this resolution, which can be considered as a point and this wire is the smallest tube in the laboratory at present. The wire is used to measure the system PSF at the depth of 50mm, which is because the cross region of the cross-tube is placed at the depth of 50mm in subsequent experimental. The resolution of the ultrasound system is measured by the averaged full width at half maximum (FWHM) value in the axial and lateral direction over 100 frames.

2.5 Super-Resolution Imaging and Velocity Mapping

The detailed parameter settings of image acquisition in this thesis are shown in table 2. In Chapter 3.3 and 3.5, the data was acquired in 800 frames. In Chapter 3.4, the data was acquired within 400, 800, 1200, 1600, 2000 and 2400 frames respectively (the corresponding data acquisition time was 0.8, 1.6, 2.4, 3.2, 4, 4.8 s) for each selected concentration shown in table 1.

Table.2. Parameter settings of image acquisition in this thesis

Pulse Repetition Frequency (PRF)	500 frames/s
Voltage of the probe	10v
Flow Rate in the tube	100 mm/s
Transmit Frequency	3.5MHz
Compounding Angles of Each Frame	7 numbers
Imaging Mode	plane wave

The model of the data acquisition and post processing used in the experiment is introduced as follows. When the emitted ultrasound waves meet the boundary, echoes will be reflected. These echoes vibrate the sensors in order to convert them into the electrical signals. After that, these signals are sampled and digitized by an analog-to-digital converter. The time gain compensation method (TGC) was used to compensate the attenuation of ultrasonic amplitude with depth.

Firstly, beamforming is applied to combine the information that is obtained from a series of array elements in order to evaluate the spatial or temporal information. Meanwhile, in the process of information synthesis, a series of weights will be added to the array echo signals to suppress the background noise and interference. The traditional delay and sum (DAS) beamforming method has the characteristics of simple synthesis and high stability. The equation is,

$$\mathrm{S_{DAS}(t)} = \sum_{\mathrm{n=0}}^{\mathrm{N-1}} w_n s_n(\mathrm{t} - \tau_{\mathrm{n}}) \quad (1)$$

Where $s_n(\mathrm{t})$ is an echo signal received by the nth element, N is the number of element, $w_n$is the weight of the nth element,τ_{n} is delay time of the nth element. The specific steps of beamforming are as follows. After radio frequency (RF) data was received by the elements, Hilbert transform was applied to obtain the complex data. Then, the method of delay and sum was added by calculating the delay according to all the pixel positions, interpolating pixel intensity and sum the value across all channel data for a single pixel. Finally, the envelope detection of the radio frequency signal was performed to produce a grayscale image that can be displayed. Envelope

detection was performed by using Hilbert Transform to transform the data into complex numbers and then taking the absolute value.

After beamforming, SVD filter was applied to remove the non-contrast agent signals of the image. The data that obtained from an ultrasound imaging system was described by a matrix A with m × n dimension into the following form,

$$A = U\Sigma V^T \tag{2}$$

Where U and V are both unit orthogonal matrices，that is $UU^T = VV^T = I$. U is the left singular matrix. V is the right singular matrix. Σonly has value on the main diagonal and other elements are zero. The values on the main diagonal are singular values. $U \in R^{m\times m}$, $\Sigma \in R^{m\times n}$, $V \in R^{n\times n}$.

$$\Sigma = \begin{bmatrix} \sigma_{11} & 0 & 0 \\ 0 & \ddots & 0 \\ 0 & 0 & \sigma_{mn} \end{bmatrix} \tag{3}$$

Where $\sigma_{11} \ldots, \sigma_{mn}$ are singular values. The key figure will be included at first singular values and secondary features will be included in the following singular values. In the ultrasound imaging, tissue signal is mainly at first singular values. The blood signal and noise signal are mainly at low singular values due to its low spatiotemporal coherence [43]. Tissue signals and noise signals are removed by only retaining the singular values associated with blood signals.

After SVD filter, localization and tracking are the two key post-processing steps to achieve the super-resolution ultrasound image and velocity map. Centroid was selected to process the localization of isolated signals. The principle of this centroiding method is to calculate the intensity weighted axial centroid of each extracted microbubble signal by selecting the amplitude corresponding to the midpoint of the length of this microbubble signal [21]. The detailed intensity weighted equation is as follows.

$$(x_c, y_c) = ([\frac{\sum_i^j x_i I_{(x_i,y_i)}}{\sum_i^j I_{(x_i,y_i)}} N_x], [\frac{\sum_i^j y_i I_{(x_i,y_i)}}{\sum_i^j I_{(x_i,y_i)}} N_y]) \tag{5}$$

Where x_c and y_c are the x-coordinate and the y-coordinate after localization using centroid method. x_i and y_i are the x-coordinate and the y-coordinate of each pixel in the selected microbubble clouds. $I_{(x_i,y_i)}$ is the intensity value corresponding to this pixel.N_x and N_y are the enlargement factor of the x-coordinate and the y-coordinate in order to obtain the super-resolution image. The symbol [] stands for taking integers. The resolution of the ultrasound super-resolution depends on the above precision of localization. In addition, the velocity and velocity direction of each microvascular can also be obtained by the super-resolution, which are calculated through the trajectory and time achieved by pairing the same microbubble in the adjacent frame.

After images were obtained, resolutions were measured to analyze. In this thesis, the resolution of the single tube and the resolution between two tubes which are imaged in the axial direction are obtained respectively. Axial resolution is the direction of the depth. Lateral resolution is perpendicular to the depth direction, and elevation resolution is perpendicular to both the axial direction and the lateral direction of the beam. The FWHM value is used to characterize the spatial resolution of ultrasound imaging.

2.6 Weight Adaptive Denoising Method Based on Morphology

Finally, a noise filtering method is developed. Mainly at lower concentrations, noises

obviously appeared after the microbubble detection, which led to the mistaken extraction of noises as microbubble clouds. These extractions further produced localization and pairing errors. To address this problem, a weight adaptive denoising method based on morphology is employed after the microbubble detection. The principle of this method is as follows. The basic morphologic transformation of mathematical morphology includes erosion (Eq. 6), dilation (Eq. 7), close operation (Eq. 8) and the open operation (Eq. 9). The equations are as follows.

$$(f \ominus g)(x) = \min_{y \in G}[f(x+y) - g(y)] \tag{6}$$

$$(f \oplus g)(x) = \max_{y \in G}[f(x-y) + g(y)] \tag{7}$$

$$(f \cdot g)(x) = [(f \oplus g) \ominus g](x) \tag{8}$$

$$(f \circ g)(x) = [(f \ominus g) \oplus g](x) \tag{9}$$

Where f(x) is the input image and g(x) is the structure element, which are two discrete functions defined on a two-dimensional discrete space F and G. This method compares the central point of a structure element with each point of the original image one by one. In the process of erosion, the minimum value is taken, which means that only the point that the structure element can be completely included in the original image is retained. That is, as long as one of the corresponding points in the structure element and original image is not 1 (1 is obtained when the corresponding points in the structure element and original image are both 1, otherwise 0.), the point is 0. So that the processed image presents the effect of shrinkage. For the dilation, the maximum value is taken, the point is retained as long as there is a point in the structure element can be included in the original picture. As long as one of the corresponding points in the structure element and original image is 1, the point is 1. Thus, the effect of expansion can be presented. Close operation is first dilation then erosion and open operation is the opposite, which can be used to remove the negative and positive pulse noise respectively. In this thesis, a denoising algorithm which consists of eight close-open cascading filters is built as shown in Fig. 5., which contains structural elements of different shapes and dimensions. Four structure elements of different shapes are connected in parallel, and those have different dimensions are connected in series. A_{nm} is the structure element, n represents the shape sequence and m represents the dimension sequence.α_i, $(i = 1 \dots 4)$ is the weight and CO is the close-open cascading filter (Eq. 10).

$$CO\big(f(x)\big) = [f \cdot g \circ g](x) \tag{10}$$

The ideal denoising effect was achieved by adjusting the shapes and dimensions of structure elements. According to the matching times of the structural elements and original image, the output weights of four parallel channels are obtained. High number of matches and high weight mean that the selected structural elements have better detection ability to the edge information of the image. The output is the weighted sum of these four channels as shown in Eq. 11.

$$F(x) = \sum_{i=1}^{4} \alpha_i f_i(x) \tag{11}$$

This filter can denoise while preserving the geometric shape of the image.

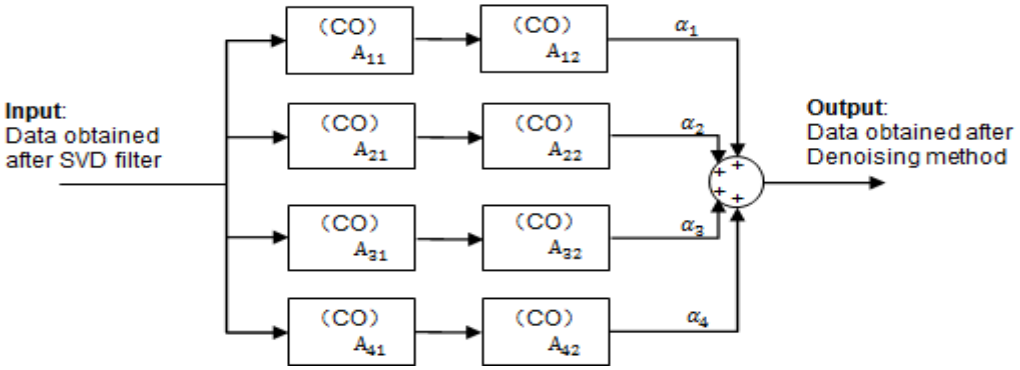

Fig. 5. Close-open cascading filter.

3. Results

3.1 Calibration of Ultrasound System

Fig. 6 (a) shows a cross-section image of the diameter of 50 microns wire at the depth of 50 mm. Fig. 6 (b) and Fig. 6 (c) show the intensity profile along the depth direction and lateral direction. The intensity profile along the depth direction and lateral direction were obtained by capturing the intensity value of each pixel that in the center column and row of the image respectively. The FWHM resolution along the depth and lateral direction are 540 microns and 1890 microns, which were the mean full width at the half maximum of the intensity profile of 100 frames.

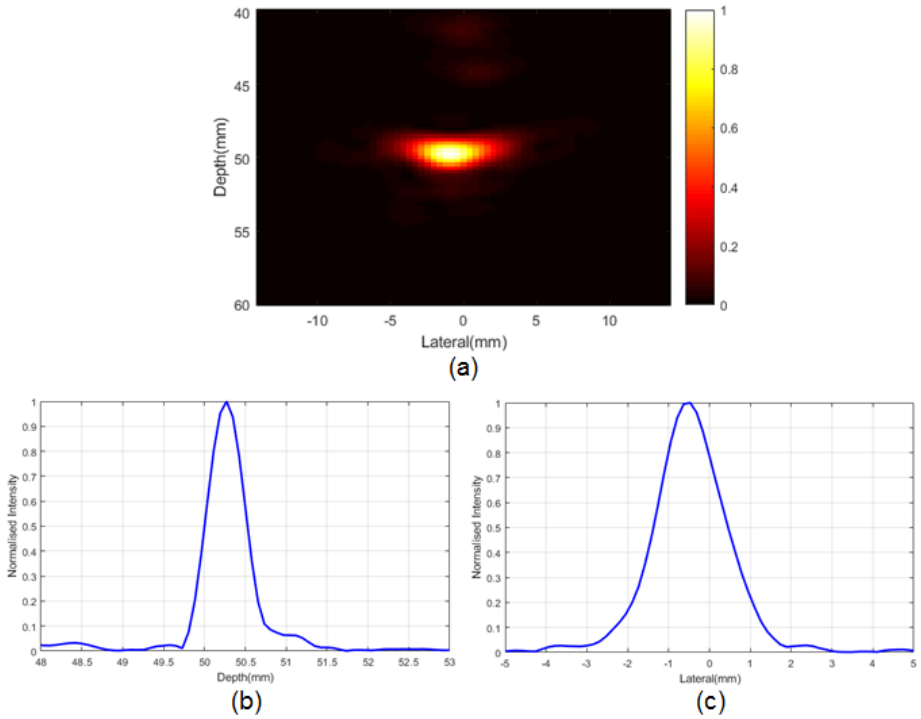

Fig. 6. (a) An exemplar image of the cross-section of the 50 microns wire. (b) The intensity profile along the depth direction through the center of mass. (c) The intensity profile along the lateral direction through the center of mass.

3.2 Super-Resolution Imaging Process

Fig. 7 shows the optical image of the cross-tube phantom. B-mode data which was based on the cross-tube phantom was obtained after the beamforming process. The first frame of the B-mode data is shown in Fig. 8. Beamforming uses ultrasound echoes to reconstruct images. This process involves determining the location and intensity information of each point. When the emitted ultrasound pulse meets the boundary of the tube and the microbubble, part of the ultrasound will be reflected back and received by the ultrasound transmitter due to the change of acoustic impedance. The transmitter used in this experiment contains 96 transmitting elements. The distance between the boundary and one transmitting element was calculated by the time of the received echo. The echo received by multiple transmitting elements was used to accurately locate the position of the boundary. The intensity at this point was obtained through envelope detection.

Fig. 7. Optical image of the cross-tube phantom with 200μm diameter

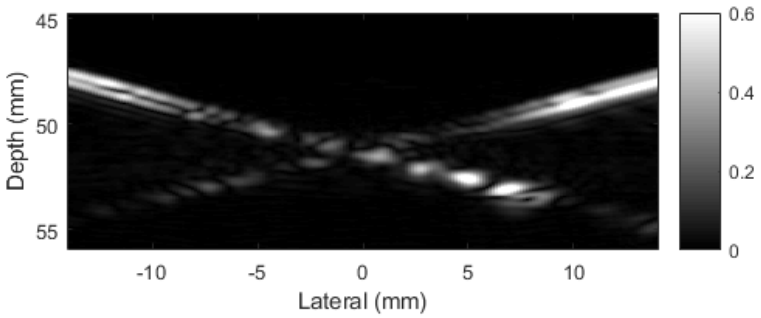

Fig. 8. The first frame of the ultrasound B-mode images based on the cross-tube phantom was obtained. The mechanism is that the diluted microbubble contrast agent flowed through the two tubes.

After beamforming, the data matrix, consisting of 800 B-mode images, was obtained. SVD filter was used to remove the non-contrast signals, which extracts moving data (representing microbubbles) and non-moving data (representing background) in different singular value intervals through singular value decomposition of image data. The image information without moving is arranged in the front, the middle is the moving image information, and the rear is noise. The reason for this phenomenon is that singular values on the diagonal in singular value decomposition are arranged from biggest to the smallest. The image features contained by singular values are arranged in order of frequency from lowest to highest. The background is low frequency. The flowing microbubble is medium frequency and the noise is high frequency. So

non-contrast agent signals can be filtered out by extracting the singular value interval in the middle region. In the process of this thesis, the matrix was reconstructed and singular values of this matrix were decomposed. Then, 800 singular values were obtained in order. A cut-off singular value range was selected to remove the signals of the tubes and the background noise. After the matrix was recovered with the selected singular values, only the signals of microbubble clouds were left in this image, as shown in Fig. 9.

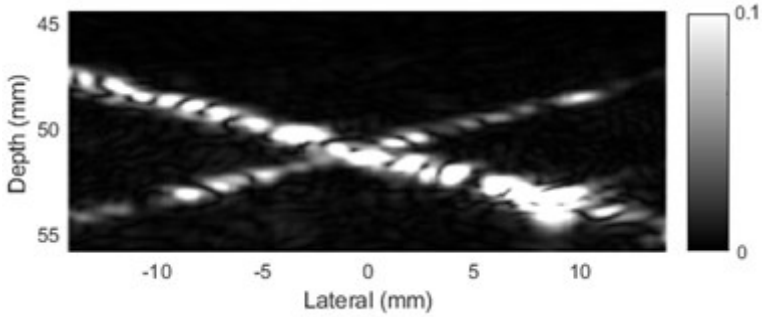

Fig. 9. The B-mode images were processed by the SVD filter. The signals of the two tubes and the background noise were removed, while only signals of microbubble clouds that placed inside the two tubes were left. It can be seen that most of these microbubble clouds are isolated, because the concentration of microbubble contrast agent was controlled in a low range.

Based on the images which were filtered by the SVD method, next steps are super localization and tracking. Super-resolution images were obtained by locating a large number of spatially independent microbubbles. The concentration of contrast agent was controlled in a low range to acquire spatially independent microbubbles. After B-mode images were obtained, all the non-contrast signals were filtered and only microbubble signals were preserved. These microbubbles were extracted and each of them was located at the area of the intensity weighted center of the mass. Although there were only a few microbubbles in each frame, with the microbubble flowing, thousands of frames were located. The clear image was formed through accumulating all of these locating points in one frame. The red circles shown in Fig.10 (a) are the process of the extraction of microbubble clouds profiles. After that, microbubble clouds which were selected are shown in Fig.10 (b). Centroiding method was used on the microbubble clouds in Fig. 10 (b) to complete the localization process, which calculated the intensity weighted center of each microbubble cloud to locate. Therefore, each isolated microbubble cloud was represented by the dot at the intensity weighted center from frame 1 to frame 800. Furthermore, all the dots were accumulated in one frame to form the super-resolution image, as shown in Fig. 10 (c), which shows the shape of the cross-tube phantom very clearly.

The velocity map in Fig. 10 (d) indicates the velocity and direction of the microbubble contrast agent that was injected into the cross-tube phantom. The velocity and direction were calculated by tracking the same microbubble cloud in the neighbouring frames. The matching of the same microbubbles was accomplished by looking for microbubbles with similar area and close distance to the reference microbubbles. The tracking method used in this experiment was to find a microbubble within the range of the area of 0.5 to 1.5 times of the reference microbubble (similar in area) and within the maximum speed limit distance from the reference microbubble (close in distance) in adjacent frames. When a microbubble met these two conditions, they were considered

as the same microbubble. Therefore, the distance of movement and the flow direction of the microbubble was obtained. The flow velocity of the microbubble in adjacent frames was obtained through the distance and pulse repetition frequency. The velocity map was acquired by calculating the velocity of all the microbubbles and accumulating them in one frame. It is observed that in the velocity map one tube is blue and another one is red, which means that microbubble clouds in the same tube have the same direction of flow and the direction in the two tubes are different. This is consistent with the ground truth.

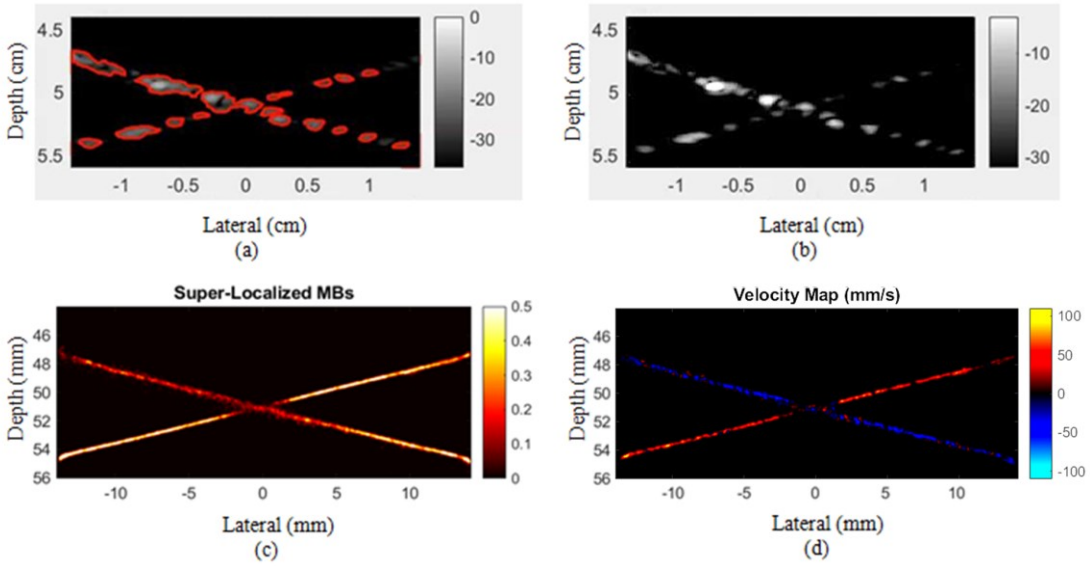

Fig. 10. (a) The extraction of microbubble clouds profiles. (b) Selected microbubble clouds which were used to locate. (c) Super-resolution image of the cross-tube phantom. (d) Velocity map of the cross-tube phantom.

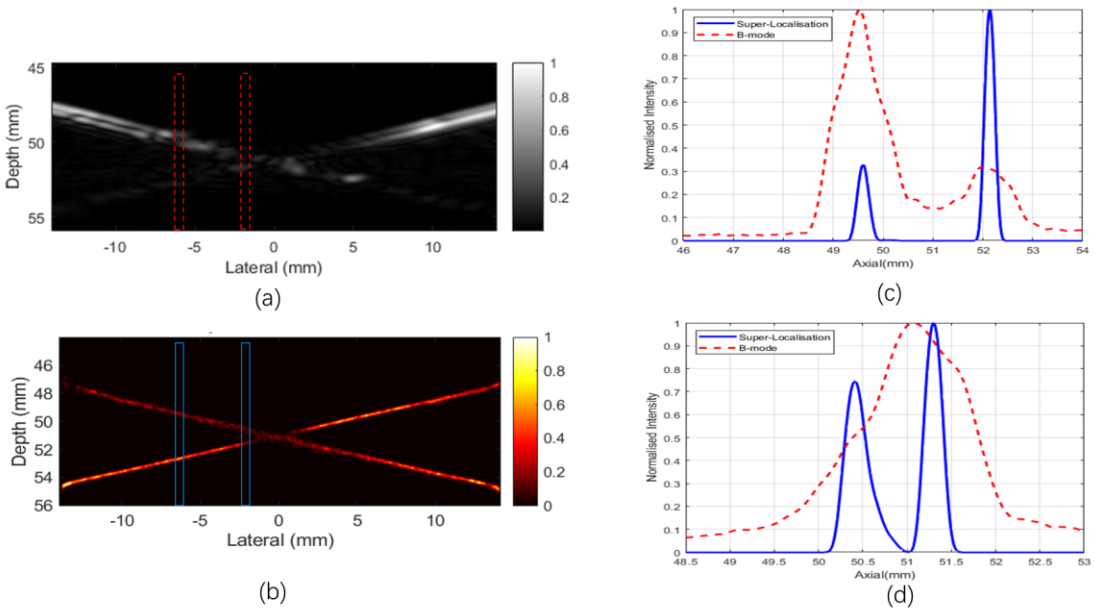

Fig. 11. (a) 800 frames of B-mode images superimposed together. (b) Super-resolution image. (c) The intensity profile in the left ROI of Super-resolution image and B-mode image. (d) The intensity profile in the right ROI of Super-resolution image and B-mode image.

Based on the B-mode image and bubble-based super-resolution ultrasound image in Fig. 10 (c), the comparison of the resolution between them is presented, as shown in Fig. 11.Fig. 11 (a) and Fig. 11 (b) show the B-mode image and the super-resolution image of the cross-tube phantom respectively. Fig. 11 (c) and Fig. 11 (d) indicate the intensity profile in the selected left (the left rectangles) and right (the right rectangles) ROI separately. The blue line and the red dotted line denote the intensity profile of ROI of super-resolution image and B-mode image separately. In Fig. 11(c), at the left ROIs of the super-resolution image and B-mode image (the blue line and dotted red line), it is observed that both of the two tubes can be separated but the FWHM value of the B-mode image is around 4.8 folds than the values for super-resolution image, which means that super-resolution image can achieve 4.8 folds higher resolution than B-mode image. As noted in Fig. 11 (d), at the right ROIs of the super-resolution image and B-mode image (the blue line and dotted red line), two tubes cannot be separated by the B-mode imaging, whereas super-resolution imaging can distinguish them by 910 μm ("peak-to-peak" distance).

3.3 Super-Resolution Images at Six Groups of Different Concentrations of 800 Frames

After the resolution comparison between the B-mode image and super-resolution image, the effect of the concentration on the resolution is studied. The microbubble contrast agent was diluted into six different concentrations ranging from 1.5×10^6 to 6×10^3particles/ml as shown in table 1. After the data acquisition and post-processing of six different concentrations were completed, super-resolution images of the cross-tube phantom were obtained in Fig. 12. It reveals that using the microbubble contrast agent with the lower concentration can produce the image of tubes with smaller diameters and distinguish two tubes near the intersection more clearly.

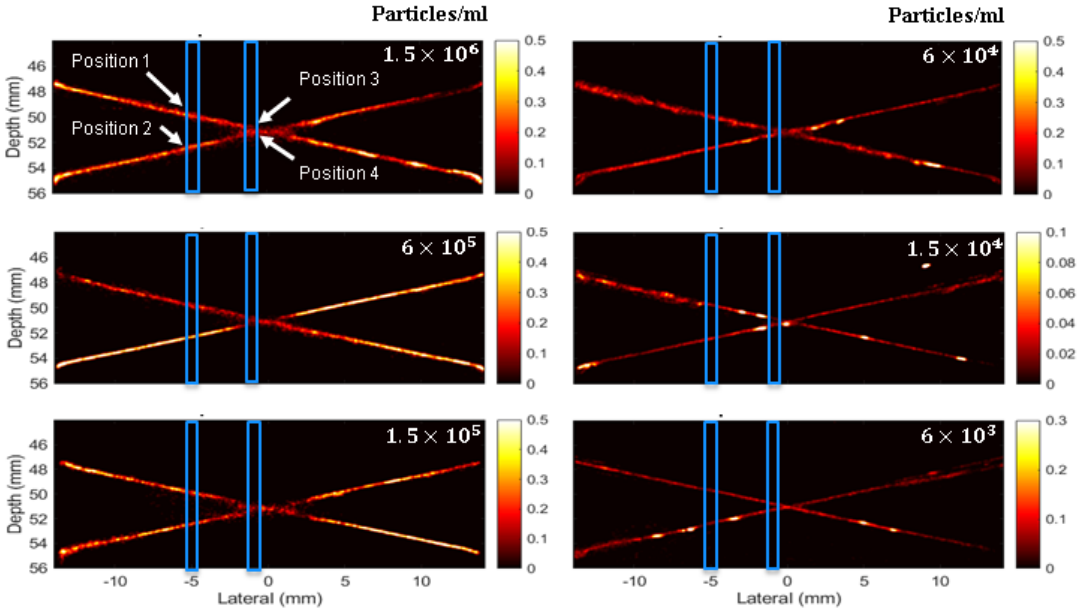

Fig. 12. Two regions of interest (ROIs) were selected in bubble-based super-resolution image at six different concentrations of 800 frames. Upper tube and lower tube in the left ROI located at position 1 and 2 respectively. Upper tube and lower tube in the right ROI located at position 3 and 4 separately.

Fig. 12 shows the bubble-based super-resolution images at six different concentrations ranging from 1.5×10^6 to 6×10^3 particles/ml. The x-axis represents the lateral distance with respect to the center of the probe. The y-axis represents the depth of the cross-tube phantom relative to the probe. In the Fig. 12, all of these six images can reveal the shape of the cross-tube phantom. In order to quantize the effect of different concentrations for microbubble-based super-resolution imaging, two ROIs (two blue boxes in Fig. 12) were selected respectively. The left ROI is the target area far away from the crossed region. Two locations were named at the left ROI, including upper tube at the position 1 and lower tube at the position 2. Then gradually shifted from the left ROI to the crossed region, the second ROI was obtained approaching to the intersection. Similarly, there are also two positions, which are the upper tube at the position 3 and lower tube at the position 4.

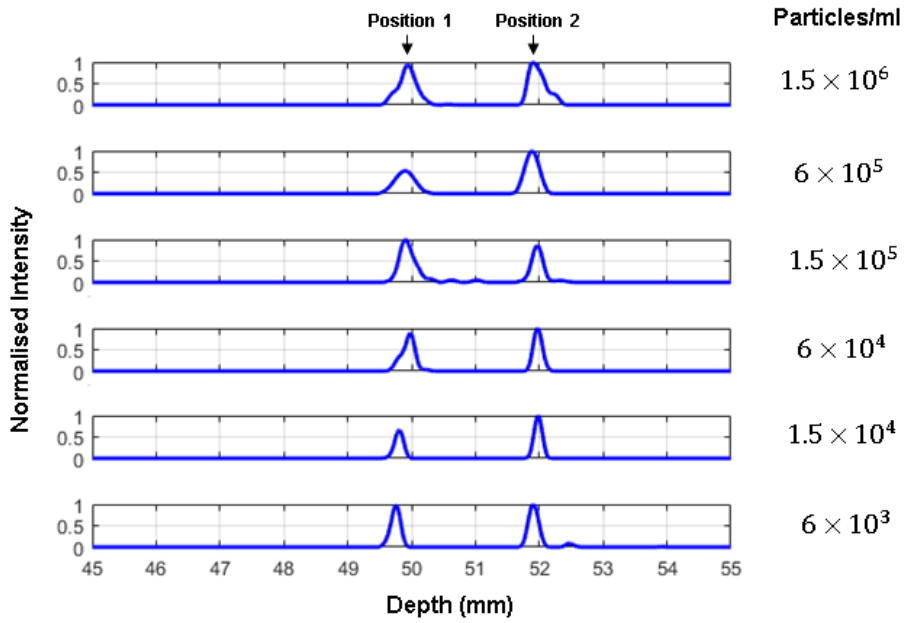

Fig. 13. The intensity profile in the left ROI of super-resolution images at six different concentrations of 800 frames is shown, including the intensity profile at position 1 and the intensity profile at position 2.

Fig. 13 shows the intensity profile of the left ROI at six concentrations. These intensity profiles specific refers to the intensity profile located at the center column of each blue box. The distance between two wave crests represents the longitudinal distance of the two tubes in the left ROI. Two waves respectively express the intensity value distribution of the two tubes at the position 1 and 2. Fig. 13 shows that when the tubes are very far away, super-resolution imaging at all of these six concentrations can distinguish these two tubes.

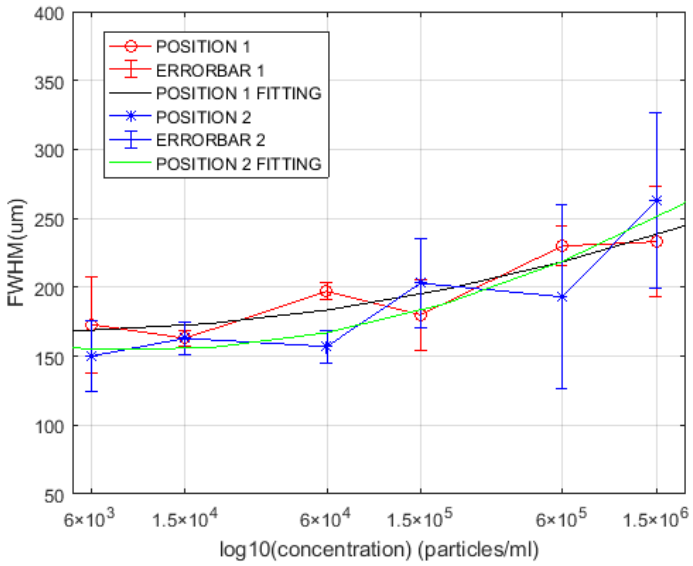

Fig. 14. FWHM values of the single tube of 800 frames at six concentrations. Log base ten of the concentration of the microbubble contrast agent as the x-axis was performed to compress the scale of the concentration value. FWHM values at the position 1 and position 2 were measured in the Fig. 13. The error bar was obtained by three repeated experiments except for the second last data at position 1. Two fitted curves were fitted using mean values.

In the Fig. 14, x-coordinate is the log base ten of six concentrations of the microbubble contrast agent. Logarithm was taken on the concentration, which aims to compress the scale of the concentration value but does not change the property and relationship between the concentration and FWHM value. Y-coordinate is the FWHM values of the single tube, which were measured in the Fig. 13. FWHM values are used to describe resolutions of the single tube at six concentrations. The data were repeated for three times except for the second last data at position 1. The data obtained from the first time is removed because it is an outlier. The figure shows the error bar of the second last data at position 1 with two repeats. On Red circles represent the FWHM values of the tube at the position 1 in the left ROI in Fig. 12 and blue circles represent the FWHM values of the tube at the position 2 at six concentrations. The inner diameter of the tube is 200±15μm. As shown in Fig. 14, all groups of concentrations correspond to FWHM values are around 200 microns. A monotonically increasing function was fitted with six discrete points at position 1 and 2 respectively. In general, the FWHM value has an increasing trend when the concentration increases. Over-fitting is prone to occur when using high-order function fitting and under-fitting is easy to occur when using low-order function fitting. These situations will cause the prediction result poor, thus a function of two orders $y = ax^2 + bx + c$ (shown in Table. 3) is used to fit these points. Two functions of two orders at the position 1 and position 2 of 800 frames are shown in Table. 1. R-square describes the variation relationship between the fitted data and original data. The value range is [0 1], and the fitting effect is best when the value equals to 1.

Table. 3. Two functions of two orders are used to fit points at position 1 and position 2 in Fig. 14 and mean values were used for fitting, which aims to obtain the variation relationship between FWHM values and concentrations.

Curve Fitting Parameters		a	b	c	Error(R-square)
800 frames	Position 1	10.26	-73.26	299.3	0.8482
	Position 2	19.84	-157.7	467.5	0.8408

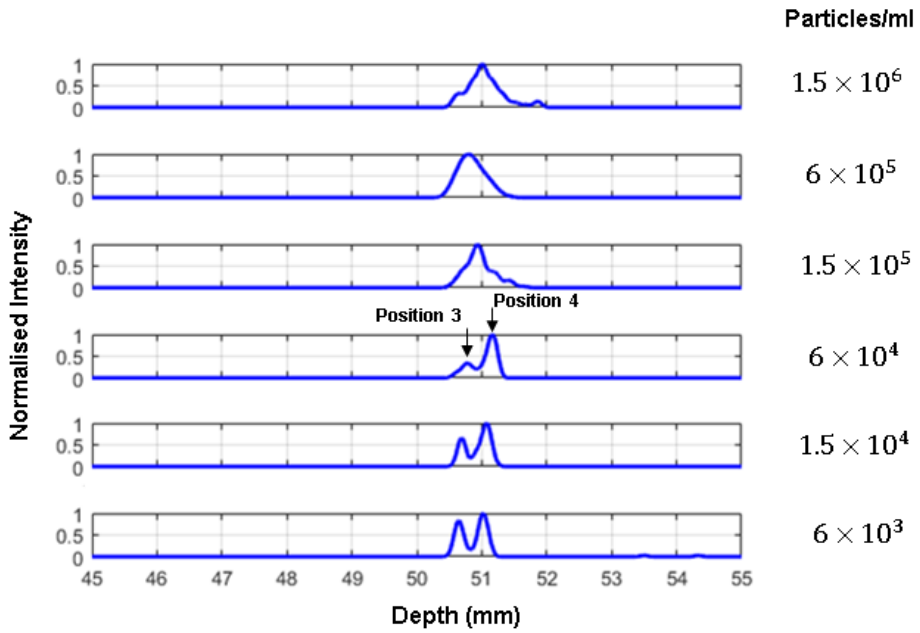

Fig. 15. The intensity profile in the right ROI of the microbubble-based super-resolution images at six concentrations of 800 frames is shown, including the intensity profile at position 3 and position 4.

Fig. 15 shows the intensity profile in the right ROI of the super-resolution image in the Fig. 12. The left crest in the last three concentrations represents the intensity profile at position 3 and the right crest represents the intensity profile at position 4. Borrowing from the Rayleigh criterion in optics, it is defined as follows: when the center of one Airy disk coincides with the first dark ring of another Airy disk, the two images can be distinguished. In this thesis, when the center of a point spread function coincides with the edge of another point spread function (about half peak), two images can be distinguished. Two tubes at position 3 and 4 cannot be distinguished by the first three higher concentrations until when the concentration decreases at 6×10^4 particles/ml, the two tubes can be identified. When the concentration decreases further, two tubes can be obviously distinguished and the two tubes are separated by 370 microns ("peak-to-peak" distance). The possible reasons for the different heights of the two peaks at different concentrations are as follows. The aggregation of microbubbles is related to the concentration. When the concentration is high, microbubbles are more likely to overlap, so that the located point will be reduced. This situation is random, so the heights of the two peaks will be different for the other concentrations. At the lowest concentration, the microbubbles are relatively independent and it is difficult to overlap. Therefore, the number of located points in the two tubes is relatively stable and the height of the two peaks will be similar.

3.4 Comprehensive Effects of Data Acquisition Time and Concentration on the Resolution of Super-Resolution Imaging

In the above experiment, the data of each concentration was collected with 800 frames (1.6s).

From these data of 800 frames, it is shown that the trend of resolution decreases when the concentration increases. Then, the comprehensive effect of data acquisition time and concentration on the super-resolution image was studied. In this thesis, the data which was collected within 0.8, 1.6, 2.4, 3.2, 4, 4.8 s (400, 1200, 1600, 2000, 2400 frames) were collected in the following experiments and previous post-processing steps were repeated. In addition, for each data acquisition time, the data was also collected at the six concentrations as shown in table 1.

The relationship of data acquisition time and the resolution between the two tubes near the intersection (in the right ROI) was shown in Fig. 16. Since two tubes can only be distinguished at concentrations of 6×10^3 particles/ml, 1.5×10^4 particles/ml and 6×10^4 particles/ml in this target region, the relationship between data acquisition time and resolution is only discussed at these three concentrations. Within the range of the study, the effect of data acquisition time on imaging resolution has a similar trend at different concentrations. The expected distance of the two tubes is 390 microns, which is measured by the protractor in a coordinate system. For the data which was obtained in the condition of these three concentrations, when the time is between 1.6 seconds and 3.2 seconds, the acquisition time has little effect on the resolution. The error of "peak-to-peak" distance remaining within the range of less than 30 microns (7.7%), which is less than the mean error of "peak-to-peak" distance 34 microns (8.7%). For the data which was obtained in the condition of 6×10^3 particles/ml with 0.8s and 4.8s data acquisition time, 1.5×10^4 particles/ml with 4.8s data acquisition time, and 6×10^4 particles/ml with 4s and 4.8s data acquisition time, a relatively large mean error around 72 microns existed, which is 18.5%. This indicates that within the studied range, the data acquisition time also has the optimal range, too long or too short will lead the error of the resolution increase. In this case, the accuracy of imaging will be affected.

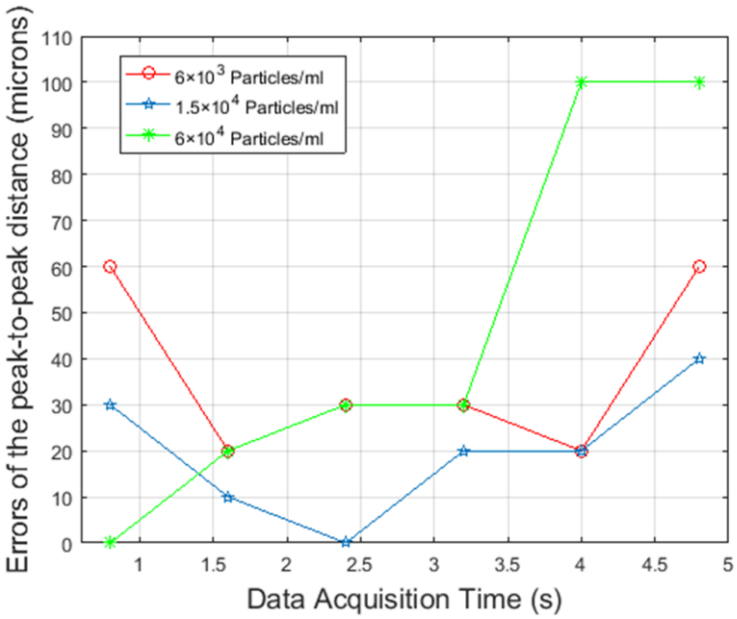

Fig. 16. The relation of data acquisition time and the resolution of the intersection of the two tubes (in the right ROI) under three concentrations is shown.

Table. 4 shows the resolution of the single tube at six concentrations and data acquisition time. Fig. 17. shows the relationship of data acquisition time and the resolution of the single tube (in the left ROI). The mean value and standard deviation (STD) of the resolution were obtained

from the data in a row or column in table 4. The values in the table are the resolutions of the single tube. Horizontally, the mean value reflects the general level of imaging resolution at the condition of the same concentration and different data acquisition time. The Table. 4 shows that under different data acquisition times, the mean value has an increasing trend with the increase of concentration, which is similar to the trend in Fig. 14. This indicates that the increase of concentration will increase the value of the resolution of the single tube. The standard deviation reflects the dispersion degree of imaging resolution at the condition of the same concentration and different data acquisition time. The dispersion degree of data increases when the standard deviation goes up. As shown in the Table. 4, the standard deviation is larger at the concentration of 1.5×10^5 particles/ml and 6×10^5 particles/ml. Fig. 17. also shows that resolution value fluctuates greatly and is unstable at these two concentrations. At the concentration of 6×10^3 particles/ml and 6×10^4 particles/ml, the resolution fluctuation is relatively stable. The red square shows the preferred concentration range and the green square shows the data which is as expected. The yellow square means the unsatisfied data. When the error is within 20.0%, it is considered to be approximate to the expected value (200 microns). For each data acquisition time with respect to different concentrations, the error of the mean resolution of the single tube with respect to the ground truth is all less than 20.0%, from 3.5% to 20.0% (shown in green squares), which means that all of them are as expected. When the error of the standard deviation is more than 20.0%, it means that the image at this data acquisition time is not stable. The table shows that 2.4 and 4 s are relatively better time which can image stably. For each concentration with respect to different data acquisition time, when the concentration is 1.5×10^6 and 6×10^3 particles/ml, the error of the mean resolution value of single tube from the true diameter is 28.0% and 22.5% respectively (shown in yellow squares). Therefore, these two concentrations do not meet the standard for a preferred concentration. When the concentration is 1.5×10^5 and 6×10^5 particles/ml, the standard deviation of the resolution is 62.38 and 58.43 microns, which is 31.4% and 29.2% (shown in yellow squares). These two errors are more than 20%, which indicates that the image is not stable at these two concentrations. Therefore, they are also not within the preferred range. When the concentration is 1.5×10^4 and 6×10^4 particles/ml, for each data acquisition time, the resolution all around the ground truth (13.5% and 16.5%) and has small standard deviation (10.3% and 5.6%), which means that they are more stable. In addition, at these two concentrations, in the intersection of the cross-tube, two tubes can also be distinguished as shown in 3.3. Therefore, the preferred choice of concentration was determined from 1.5×10^4 to 6×10^4 particles/ml as shown in red squares in table 4.

Table. 4 Comprehensive effects of data acquisition time and concentration on resolution of the single tube

Time (s) / Concentration (Particles/ml)	0.8	1.6	2.4	3.2	4	4.8	Mean	Error (mean)	STD	Error (STD)
6×10^3	150	180	140	140	150	170	155	22.5%	15.00	7.5%
1.5×10^4	150	150	210	210	180	170	173	13.5%	20.55	10.3%
6×10^4	150	170	160	160	180	160	167	16.5%	11.06	5.6%
1.5×10^5	260	180	240	240	200	190	232	16.0%	62.83	31.4%
6×10^5	260	270	150	150	150	270	208	4.0%	58.43	29.2%
1.5×10^6	270	300	230	270	200	320	256	28.0%	40.31	20.2%
Mean	207	208	188	180	176	240				
Error (mean)	3.5%	4.0%	6.0%	10.0%	12.0%	20.0%				
STD	56.76	55.80	39.75	42.82	20.55	77.03				
Error (STD)	28.4%	27.9%	19.9%	21.4%	10.3%	38.5%				

Unit: Microns

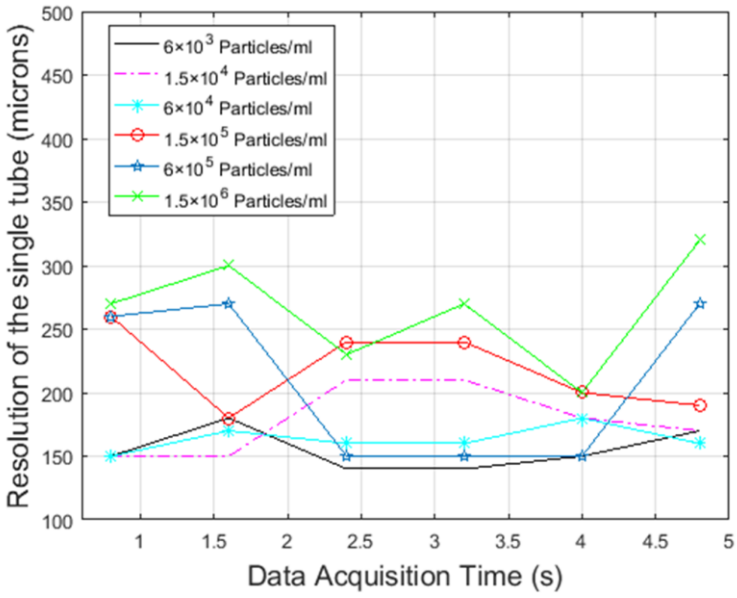

Fig. 17. The relation of data acquisition time and the resolution of the single tube (in the left ROI) under six concentrations is shown.

As for the effect of the data acquisition time, in some cases, the time of data acquisition is not the longer the better. When the time of data acquisition rises, the amount of obtained data increases but errors will also exist in the accumulation. These errors could be caused by the effect of artifacts and noises on the image. Especially for the lower concentrations, this effect may be more obvious because the number of signals of microbubble clouds is low. In addition, some microbubble clouds may also stick to the wall of the tube and move slowly. This situation also has a bigger effect for lower concentrations.

Take 1.6s and 4.8s (800 and 2400 frames) as an example, for the higher concentration, the super-resolution image becomes more continuous (shown in white boxes in the Fig. 18 (b)) due to the increasing of valid data. However, the local image quality at low concentration may become worse, such as shown in yellow boxes in the Fig. 18 (b), this may because that microbubble clouds are easy to suddenly move or attach along the wall of the tube. It's even more obvious at lower concentrations. The slow flow of some microbubbles will cause localization to be very concentrated, which leads to some bright points in the image. This situation will reduce the overall imaging effect. In addition, the SVD filter is data driven, which means that different data will have different filtering effects. When the frame of data increases, the noise generated after filtering will accumulate more. Although increasing the time of data acquisition can obtain more valid data, the effect of noise that is difficult to filter may result in obtaining more unsatisfactory image.

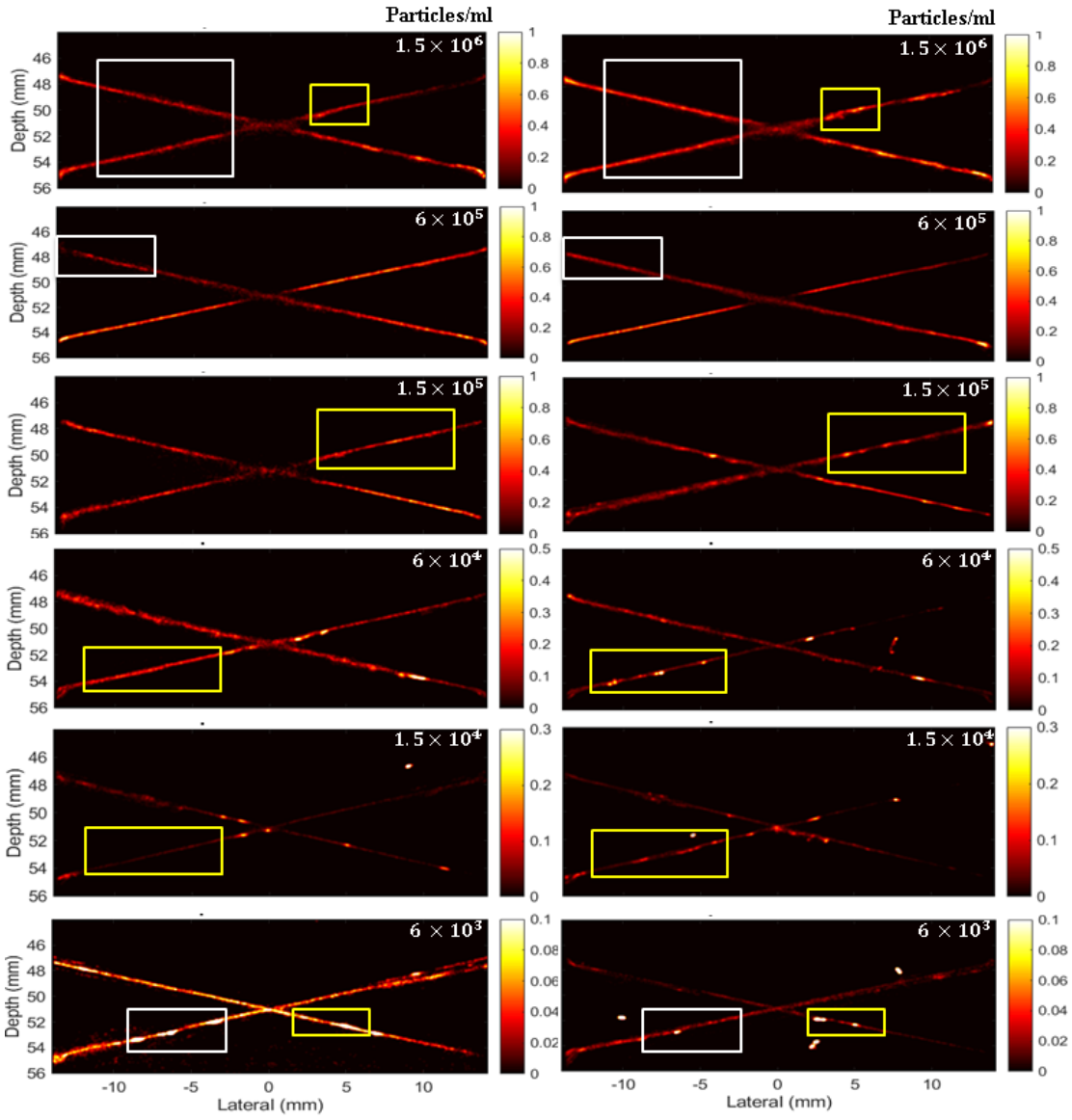

(a) (b)

Fig. 18. Microbubble-based super-resolution images of (a) 1.6s and (b) 4.8s at six concentrations are shown. White boxes show the improvement and yellow boxes show the deficiency of local image quality in 4.8s in comparison to 1.6s.

3.5 Noise Filtering on Six Groups of Different Concentrations of 800 Frames

The weight adaptive denoising method based on morphology was performed on the data of six different concentrations of 800 frames. The bubble image without denoising algorithm is shown in Fig. 19 (a). In the yellow box of Fig. 19 (b), it shows that noises are removed very effectively after applying denoising algorithm.

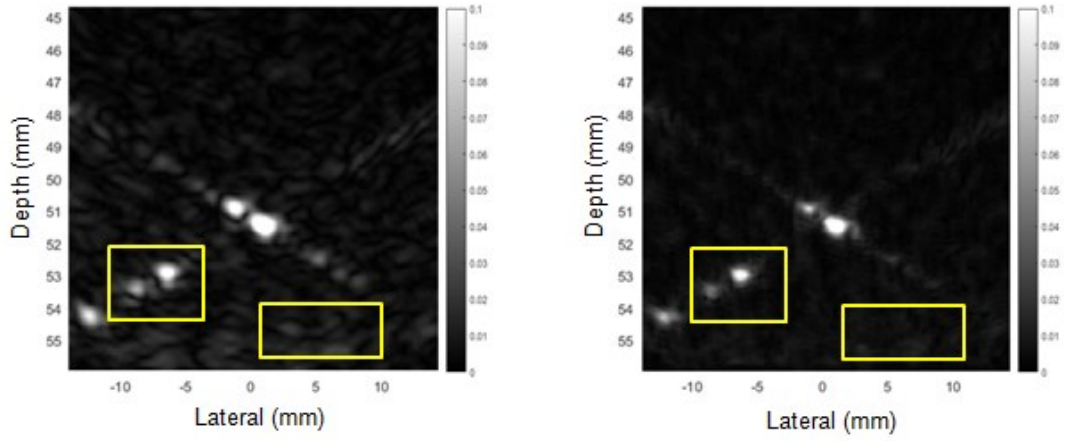

(a) (b)

Fig. 19. (a) shows the bubble image without denoising algorithm. (b) shows the bubble image after denoising algorithm.

Fig. 20 shows that super-resolution images at the lower two concentrations of microbubble contrast agent are significantly enhanced applying the denoising algorithm (the improved algorithm). As shown in the white boxes in the Fig. 20 (b), localization errors which are caused by noises in the image, such as double lines and impurity on the outside of the tube, were effectively removed. But there are few improvements for the higher concentration, such as the 1.5×10^6 particles/ml as shown the first line in the Fig. 20.

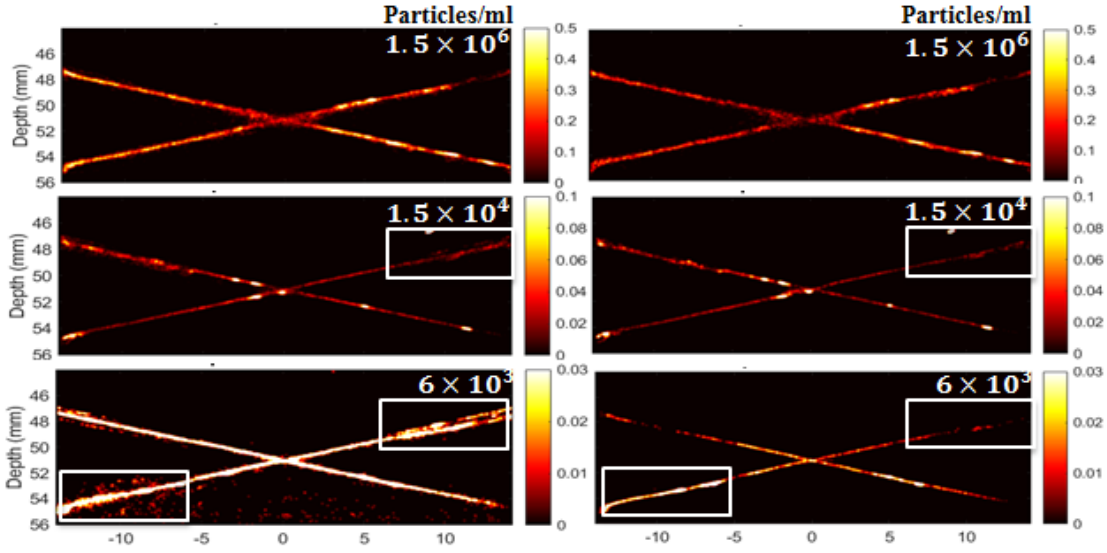

(a) (b)

Fig. 20. Each column shows super-resolution images with the (a) original algorithm and (b) improved algorithm respectively.

Although the image quality is not improved at the higher concentration, the resolution at the position 3 and 4 in the right ROI are significantly enhanced by the improved algorithm, especially for the higher three concentrations. In Fig. 21, two tubes which were in the selected right ROI can be distinguished by the average 340 microns (“peak-to-peak” distance) at all the concentrations. In fig. 22, it is obviously observed that the super-resolution image under the improved algorithm can

separate the two tubes at all the selected concentrations, but the original one can only distinguish them when the concentration is as low as 6×10^4 particles/ml.

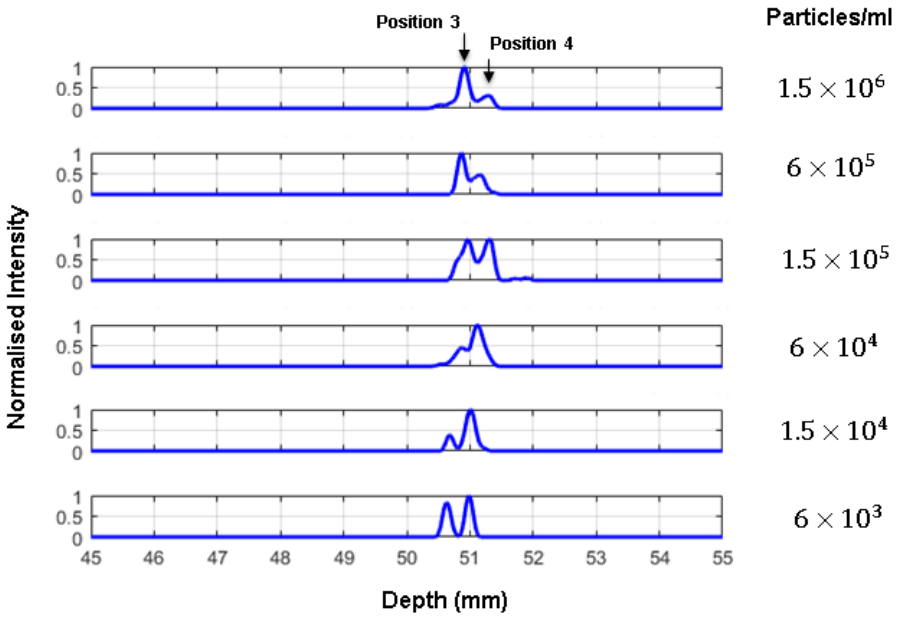

Fig. 21. The intensity profile at the right ROI at six concentrations of 800 frames which were processed by the improved algorithm is shown, including the intensity profile at position 3 and the intensity profile at position 4.

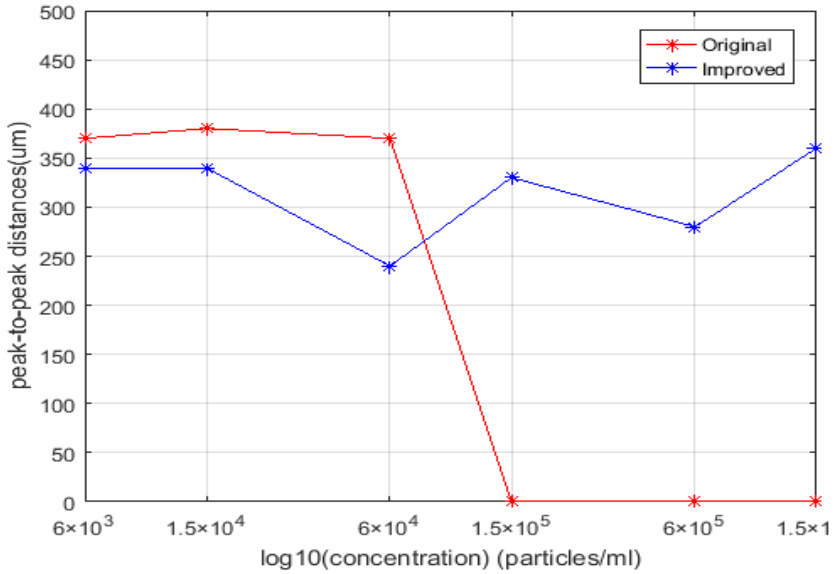

Fig. 22. Peak-to-peak distance of the two tubes at the position 3 and 4 respectively are shown under the original algorithm and the improved algorithm, which were obtained from Fig. 15 and Fig. 21.

In addition to the enhancement in super-resolution images, for the velocity map, there are also some improvements for the lower concentrations. In the white boxes of the improved algorithm in Fig. 23, it shows that velocity map is significantly enhanced by the improved algorithm. Red line represents that microbubbles flow in one direction, and blue line shows that microbubbles flow in another direction. Microbubbles in the same tube should flow in the same direction. However, in the white box of original algorithm in Fig. 23, some noises which were

mistaken for microbubbles lead to the wrong calculation of the velocity direction. This situation causes that there are red and blue dots in the same tube, which means that there are different flow directions in one tube. This is not match with the ground truth.

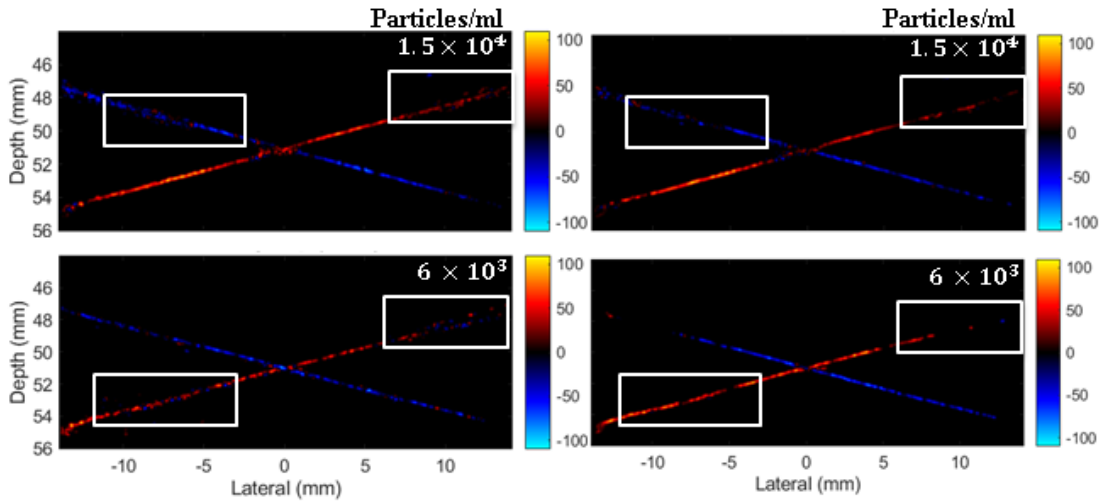

(a) (b)

Fig. 23. Each row shows the velocity map at the lower concentrations, at the 1.5×10^4 and 6×10^3 particles/ml. Each column is obtained by the (a) original algorithm and (b) improved algorithm respectively.

4. Discussion

The effect of the concentration on the microbubble-based ultrasound super-resolution imaging was investigated in this thesis by establishing a microvasculature phantom for experimental validation. The result in 3.3 shows that reducing the concentration can increase the resolution of the microbubble-based ultrasound super-resolution imaging at the intersection by reducing the localization position errors. The result in 3.4 shows the comprehensive effects of data acquisition time and concentration on imaging resolution. 3.5 shows the effect of the denoising method.

Localization may be affected by various factors. The point spread function of the system will affect the profile and signal strength of microbubble clouds. Microbubble clouds may change as they flow in the cross-tube phantom, including coalescence, shrinking and fragmentation. Furthermore, microbubble clouds may flow along the elevational direction of the probe and deviate from the imaging plane. For using the 2D imaging, the imaging edge of the microbubble clouds will be changed by these deviations. The change of irregularly shape of the microbubble cloud will cause the localization position jump occurred, which will give rise to localization errors. Moreover, it causes a certain amount of interference for the tracking of the bubble clouds, especially for the situation of high concentration imaging.

In Fig. 14, it shows the growing trend of the resolution when the concentration decreases. The variation of the resolution rises when the span of the selected concentration increases. When the concentration span is small, the change of resolution is slightly weaker. Moreover, among the lower three concentrations, there is a little change in resolution. The reason of this phenomenon

could be that the resolution is associated with concentration selection. For the lowest concentration, the resolution is slightly reduced, which can be considered as within the margin of error without affecting the overall trend.

In the experiment, the concentration of the microbubble contrast agent remained stable by a stirrer so that microbubbles can distribute as evenly as possible. However, at present, due to the limitation of the experimental equipment, it is impossible to observe changes of the concentration when microbubbles flow into the cross-tube phantom. Thus, the experiment results may be influenced to some extent and this could be the reason of the outlier (position 1 at 6×10^5 particles/ml in Fig. 14). In the ultrasound imaging, the strength of the microbubble cloud signal is related with the properties of bubble clouds themselves, including density, shape, size and the position relative to the probe and surrounding wall of the tube.

For the noise filtering algorithm, there are also some limitations. There are few improvements for the super-resolution images that were obtained at higher concentrations. Same with these super-resolution images, the improved algorithm is unable to improve the velocity map at higher concentrations as well. Fig. 24 shows that the velocity map obtained by the improved algorithm has even a little worse effect (shown in white boxes) at higher concentrations, such as the 1.5×10^6 particles/ml. This may because that for the high concentrations, the signals of microbubble clouds are relatively close to each other. The function of the close operation of the denoising method is to fill in the small gap in the image. The space between two microbubble clouds that is too close together will be mistaken for a small gap that needs to be filled in, and thus mistaken for one microbubble cloud, such as shown in the yellow boxes of Fig. 25. Therefore, errors of localization and tracking increase after using this denoising filter.

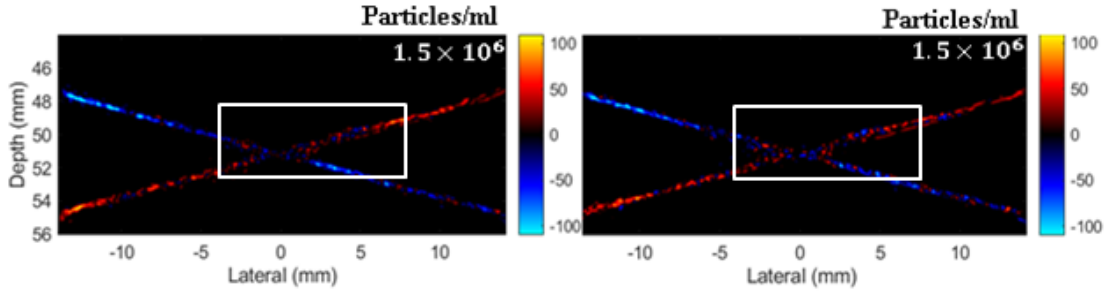

(a) (b)

Fig. 24. The row shows the velocity map at the 1.5×10^6 particles/ml (the higher concentration). The velocity map was obtained by the (a) original algorithm and (b) improved algorithm respectively.

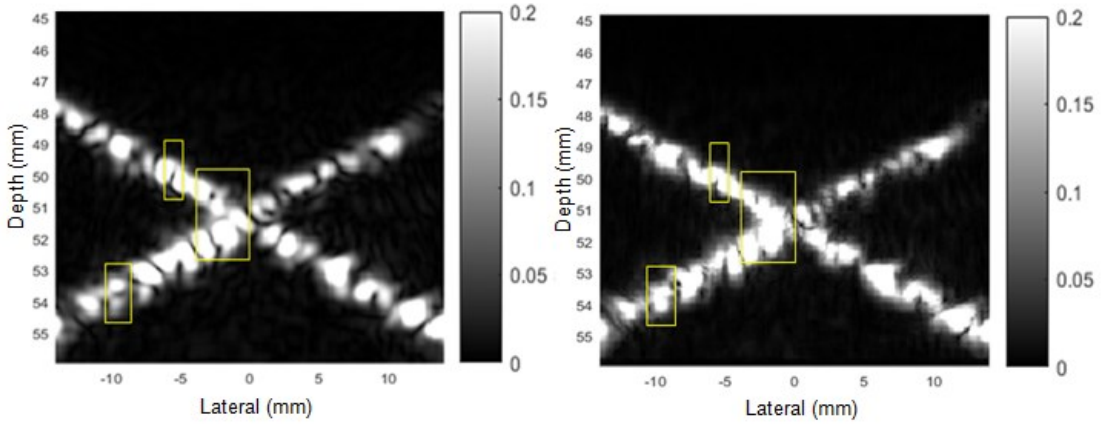

(a) (b)

Fig. 25. The row shows the microbubble detection images at the 1.5×10^6 particles/ml (the higher concentration). The image is obtained by the (a) original algorithm and (b) improved algorithm respectively.

5. Conclusion

This thesis mainly studied the effect of the agent concentration in super-resolution imaging at the clinical low frequency. Firstly, the effect of the concentration of the microbubble contrast agent on the super resolution imaging was proved by experiments. On this basis, the comprehensive effects of concentration and data acquisition time on the resolution are analyzed in order to obtain the preferred concentration range. In addition, a denoising method for super-resolution imaging is developed to improve the signal processing in super resolution imaging. Therefore, the resolution of the imaging, the accuracy of imaging and velocity map can be further improved. By improving the resolution of super-resolution imaging, the ability to distinguish between adjacent microvessels can be enhanced, so as to make more accurate imaging of the microvessels within the tumor, and realize auxiliary diagnosis and treatment monitoring.

In this thesis, a cross-tube phantom was fabricated to simulate adjacent microvessels. The microbubble contrast agent was prepared and diluted into 6 groups of concentrations (1.5×10^6,6×10^5,1.5×10^5,6×10^4,1.5×10^4, 6×10^3 particles/ml). Then, these contrast agents at different concentrations were injected into the cross-tube phantom separately. For each concentration, six different data acquisition times were selected (0.8, 1.6, 2.4, 3.2, 4, 4.8 s). The experiment data was obtained by the probe P4-1v with the ultrasound research platform (Verasonics Vantage 128) at a depth of 5 cm from the center of the cross-tube. After the data was collected, the super-resolution images under different contrast agent concentrations were obtained by post-processing. The post-processing steps include beamforming, SVD filter, denoising, localization and tracking. Among them, beamforming, SVD filter, localization, tracking are commonly used steps, and denoising is one of the contributions of this thesis. The effect of concentration on super-resolution imaging was compared by analyzing the resolution in the selected region of interest. The comprehensive effects of concentration and data acquisition time on resolution, and the preferred concentration range was determined by the errors of the peak-to-peak distance and the mean and standard deviation of the resolution. Finally, the denoising

algorithm was verified by comparing the images which are processed by the original algorithm with those adding the denoising algorithm.

In this thesis, two tubes of 200 microns diameter were used to simulate the microvessels. Two tubes were placed in an intersecting position to simulate the adjacent microvessels, so as to facilitate the comparison of resolution under different imaging conditions (different concentrations of microbubble contrast agent and data acquisition times). The microbubble contrast agent was made by injecting Octafluoropropane gas into a vial of lab-prepared lipid colloid for 30s. Then a bubble shaker was used to agitate the vial at 4000 r/min for 60s. The advantage of this microbubble contrast agent is that it is simple to fabricate and can form microbubbles quickly. In addition, the microbubbles can last for enough time and have high backscattered signals, which are beneficial to ultrasound imaging. Furthermore, the microbubbles are biocompatible. Microbubbles have diameters less than 10 microns, which can allow them to enter microvessels of diameters of 60 microns. The diluted microbubble contrast agents were injected into the cross-tube phantom through two syringes, which were controlled by an electric pump. The ultrasound imaging equipment used in this thesis is P4-1v probe and ultrasound research platform. The imaging parameters were set as plane wave, 10v voltage, transmission frequency 3.5MHz, pulse repetition frequency 500Hz, and in-tube flow rate 100mm/s.

This thesis has the following three contributions. Firstly, the effects of concentrations of microbubble contrast agents on super-resolution imaging is studied experimentally. Various concentrations of microbubble contrast agents were injected into the cross-tube flow phantom and the results show that in the above concentration range, a lower microbubble concentration will improve the resolution of the intersection of the cross-tube. By comparing the resolution at the region of interest near the intersection, it is found that when the concentration is lower than the 1.5×10^5 particles/ml, two tubes in the region of interest near the intersection that are 370 microns apart can be separated, which is close to the expected distance (390 microns). The error of this resolution is 5.1%.

Secondly, the comprehensive effects of data acquisition time and concentration on imaging resolution were studied. The above diluted concentrations were used. For each concentration, six data acquisition time were selected respectively. On the whole, there are 36 sets of data were collected for analysis. When the data acquisition time is 4.8s and the concentration is 6×10^3 particles/ml, there is a large bias in the resolution of two tubes in the right ROI, which is 22.3%. The preferred microbubble concentration range was determined between 6×10^4 and 1.5×10^4 particles/ml within the studied range. At these concentrations, the error of the mean value of the resolution of the single tube is between 13.5% and 16.5%. The standard deviation of the resolution is between 5.6% and 10.3%.

Finally, the weight adaptive denoising method based on morphology was developed in the super-resolution ultrasound imaging. The principle is that by convolving the original image with structural elements, the original image is dilated and eroded to remove noise. The effect of this denoising algorithm was verified by comparing the images processed by the original algorithm with the improved one. For low concentration contrast agent imaging, including preferred range of the concentration, it can effectively remove noises that could be mistaken for microbubbles. Therefore, the resolution of the intersection of the cross-tube, and the accuracy of the image and velocity map were further improved.

There are also some limitations of this thesis. Firstly, reducing the concentration to improve

the resolution is limited because low concentration of contrast agent requires relatively long data acquisition time. There is a tradeoff between data acquisition time and concentration. Secondly, for the denoising method used in this thesis, when the concentration is high, there are few improvements because this denoising method can fill in small gaps in the image. When the concentration is high, the distance between two microbubble clouds is very close. This denoising method will fill in this distance to make these two microbubbles into one. This situation causes localization errors in the super-resolution imaging.

6. Future Work

For the future work, 3D super-resolution imaging is worth studying in the future research. The current imaging method needs to ensure that the cross-tube and probe are in the same plane. In this case, microbubbles that deviate from the plane cannot be tracked. The clinical situation is very complex, 3D imaging can solve this problem in some degree and is able to visualize more complex and disordered structure of microvasculature. Moreover, the effect of concentration on quality of super-resolution images can be further studied in more realistic situations, such as tissue and tissue motion or in vivo in the future. The diameter of the microvessel is generally less than 60 microns. In order to simulate the microvessel more realistically, a smaller diameter tube can be used in the future research. In this case, the preferred concentration range will change. Furthermore, at present, for the process of microbubble profile extraction, it needs to try many times to find whether the selected threshold can extract the profile of the microbubble. Especially for different data sets, it needs great deal of attempts to select the appropriate threshold. The threshold usually depends on the experience of researchers. Therefore, a selection method of this threshold is worth to develop. Usually, the FWHM distance is identified as the resolution of the ultrasound system when measuring the characteristics of the system and it is proportional to the real distance. Therefore, this can be potential used to deal with this problem. In addition, it is also necessary to study how long microbubbles can survive under ultrasound wave. When the flow rate is very slow, the microbubbles will be under the ultrasound wave for a long time, which may cause the microbubble to disappear. This will result in the uncontrollable deviation between the set concentration and the actual concentration. In this case, the tracking error of the microbubbles will also appear. Therefore, the survival time of microbubbles under ultrasound waves at low or no flow rates can be studied.

Reference

[1] Yu J, Lavery L, Kim K. Super-resolution ultrasound imaging method for microvasculature in vivo with a high temporal accuracy[J]. Scientific reports, 2018, 8(1): 1-11.

[2] Brown J, Christensen-Jeffries K, Harput S, et al. Investigation of microbubble detection methods for super-resolution imaging of microvasculature[J]. IEEE transactions on ultrasonics, ferroelectrics, and frequency control, 2019, 66(4): 676-691.
[3] Christensen-Jeffries K, Browning R J, Tang M X, et al. In vivo acoustic super-resolution and super-resolved velocity mapping using microbubbles[J]. IEEE transactions on medical imaging, 2014, 34(2): 433-440.
[4] Hoskins, Peter R., Kevin Martin, and Abigail Thrush, eds. Diagnostic ultrasound: physics and equipment. Cambridge University Press, 2010.
[5] Christensen-Jeffries K, Couture O, Dayton P A, et al. Super-resolution ultrasound imaging[J]. Ultrasound in Medicine & Biology, 2020.
[6] Tanter M, Fink M. Ultrafast imaging in biomedical ultrasound[J]. IEEE transactions on ultrasonics, ferroelectrics, and frequency control, 2014, 61(1): 102-119.
[7] Zhu J, Lin S, Leow C H, et al. High Frame Rate Contrast-Enhanced Ultrasound Imaging for Slow Lymphatic Flow: Influence of Ultrasound Pressure and Flow Rate on Bubble Disruption and Image Persistence[J]. Ultrasound in medicine & biology, 2019, 45(9): 2456-2470.
[8] Stanziola A, Leow C H, Bazigou E, et al. ASAP: Super-contrast vasculature imaging using coherence analysis and high frame-rate contrast enhanced ultrasound[J]. IEEE transactions on medical imaging, 2018, 37(8): 1847-1856.
[9] Hyun D, Trahey G E, Dahl J J. Real-time high-framerate in vivo cardiac SLSC imaging with a GPU-based beamformer[C]//2015 IEEE International Ultrasonics Symposium (IUS). IEEE, 2015: 1-4.
[10] Montaldo G, Tanter M, Bercoff J, et al. Coherent plane-wave compounding for very high frame rate ultrasonography and transient elastography[J]. IEEE transactions on ultrasonics, ferroelectrics, and frequency control, 2009, 56(3): 489-506.
[11] Ghosh D, Xiong F, Sirsi S R, et al. Toward optimization of in vivo super‐resolution ultrasound imaging using size‐selected microbubble contrast agents[J]. Medical physics, 2017, 44(12): 6304-6313.
[12] Cosgrove D. Ultrasound contrast agents: an overview[J]. European journal of radiology, 2006, 60(3): 324-330.
[13] Errico C, Pierre J, Pezet S, et al. Ultrafast ultrasound localization microscopy for deep super-resolution vascular imaging[J]. Nature, 2015, 527(7579): 499-502.
[14] O'Reilly M A, Hynynen K. A super-resolution ultrasound method for brain vascular mapping[J]. Medical physics, 2013, 40(11).
[15] Couture O, Besson B, Montaldo G, et al. Microbubble ultrasound super-localization imaging (MUSLI)[C]//2011 IEEE International Ultrasonics Symposium. IEEE, 2011: 1285-1287.
[16] Lin F, Shelton S E, Espíndola D, et al. 3-D ultrasound localization microscopy for identifying microvascular morphology features of tumor angiogenesis at a resolution beyond the diffraction limit of conventional ultrasound[J]. Theranostics, 2017, 7(1): 196.
[17] Foiret J, Zhang H, Ilovitsh T, et al. Ultrasound localization microscopy to image and assess microvasculature in a rat kidney[J]. Scientific reports, 2017, 7(1): 1-12.
[18] Siepmann M, Schmitz G, Bzyl J, et al. Imaging tumor vascularity by tracing single microbubbles[C]//2011 IEEE International Ultrasonics Symposium. IEEE, 2011: 1906-1909.
[19] Harput S, Christensen-Jeffries K, Li Y, et al. Two stage sub-wavelength motion correction in human microvasculature for ceus imaging[C]//2017 IEEE International Ultrasonics Symposium

(IUS). IEEE, 2017: 1-4.
[20] Bar-Zion A, Solomon O, Tremblay-Darveau C, et al. SUSHI: Sparsity-based ultrasound super-resolution hemodynamic imaging[J]. IEEE transactions on ultrasonics, ferroelectrics, and frequency control, 2018, 65(12): 2365-2380.
[21] van Sloun R J G, Solomon O, Bruce M, et al. Super-resolution ultrasound localization microscopy through deep learning[J]. arXivpreprint arXiv:1804.07661, 2018.
[22] Christensen-Jeffries K, Harput S, Brown J, et al. Microbubble axial localization errors in ultrasound super-resolution imaging[J]. IEEE transactions on ultrasonics, ferroelectrics, and frequency control, 2017, 64(11): 1644-1654.
[23] Ackermann D, Schmitz G. Detection and tracking of multiple microbubbles in ultrasound B-mode images[J]. IEEE transactions on ultrasonics, ferroelectrics, and frequency control, 2015, 63(1): 72-82.
[24] Song P, Trzasko J D, Manduca A, et al. Improved super-resolution ultrasound microvessel imaging with spatiotemporal nonlocal means filtering and bipartite graph-based microbubble tracking[J]. IEEE transactions on ultrasonics, ferroelectrics, and frequency control, 2017, 65(2): 149-167.
[25] Tang S, Song P, Trzasko J D, et al. Kalman Filter–Based Microbubble Tracking for Robust Super-Resolution Ultrasound Microvessel Imaging[J]. IEEE transactions on ultrasonics, ferroelectrics, and frequency control, 2020.
[26] Zhang G, Harput S, Lin S, et al. Acoustic wave sparsely activated localization microscopy (AWSALM): Super-resolution ultrasound imaging using acoustic activation and deactivation of nanodroplets[J]. Applied Physics Letters, 2018, 113(1): 014101.